NANO LETTERS

pubs.acs.org/NanoLett Letter

Multicone Diamond Waveguides for Nanoscale Quantum Sensing

Tianqi Zhu, Jan Rhensius, Konstantin Herb, Viraj Damle, Gabriel Puebla-Hellmann, Christian L. Degen,* and Erika Janitz*

Cite This: *Nano Lett.* 2023, 23, 10110–10117 Read Online

ACCESS | Metrics & More | Article Recommendations | Supporting Information

ABSTRACT: The long-lived electronic spin of the nitrogen-vacancy (NV) center in diamonds is a promising quantum sensor for detecting nanoscopic magnetic and electric fields in various environments. However, the poor signal-to-noise ratio (SNR) of prevalent optical spin-readout techniques presents a critical challenge in improving measurement sensitivity. Here, we address this limitation by coupling individual NVs to optimized diamond nanopillars, thereby enhancing the collection efficiency of fluorescence. Guided by near-field optical simulations, we predict improved performance for tall ($\geq$5 μm) pillars with tapered sidewalls. This is subsequently verified by fabricating and characterizing a representative set of structures using a newly developed nanofabrication process. We observe increased SNR for optimized devices, owing to improved emission collimation and directionality. Promisingly, these devices are compatible with low-numerical-aperture collection optics and a reduced tip radius, reducing experimental overhead and facilitating improved spatial resolution for scanning applications.

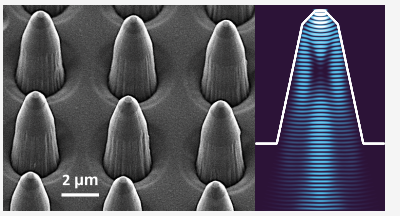

KEYWORDS: *nitrogen-vacancy center, diamond nanophotonics, diamond nanofabrication, quantum sensing, multicone nanopillar*

Electronic spins associated with individual atomic defects in wide-bandgap materials[1] can serve as magnetic sensors with exquisite sensitivity and nanoscale spatial resolution.[2] Notably, near-surface nitrogen-vacancy (NV) centers in diamond[3] have been harnessed to image exotic magnetic materials,[4,5] nanoscale currents,[6] and single- to few-molecule samples.[7] Such experiments profit from the exceptional spin coherence of the NV, which can exceed 1 ms at room temperature[8] and 1 s at cryogenic temperatures.[9] In addition, the spin state can be efficiently initialized with a laser[10] and manipulated with microwave fields.[11] Despite their promise, measurement sensitivities for near-surface NVs are hampered by poor signal-to-noise ratios (SNRs) for optical spin readout.[12] SNR scales with the square root of the collected fluorescence, which is limited by the high refractive index of diamond (n_d = 2.4), causing total internal reflection for emission outside of a critical angle of ≈25°.[13] Consequently, improved directionality and collimation of the NV emission are highly desirable.

Recent progress in nanophotonics[14] addresses this challenge by coupling fluorescence to optical structures.[15] This progress can be divided into two categories: (1) hybrid nanophotonics, including structures fabricated from alternative materials that are interfaced with diamond, and (2) diamond nanophotonics, where optical devices are carved into the diamond itself. Hybrid approaches may benefit from mature fabrication techniques available for, e.g., metals,[16] silica,[17] Si,[18] and III–V materials.[19,20] However, such structures often exhibit reduced coupling to NV emission,[21] and the presence of additional materials may reduce proximity to sensing targets.[22]

In contrast, diamond optical structures facilitate maximum coupling to NV centers and proximity to sensing targets. Recent nanofabrication advances[23−25] have paved the way for creating bespoke diamond devices such as lenses,[26,27] gratings,[28] optical cavities,[23,24,29] and waveguides.[30,31] In particular, nanoscale pillars containing shallow NVs have garnered attention for sensing applications. These devices act as waveguides for NV fluorescence, enhancing broadband collection efficiency. In addition, ∼100 nm device diameters facilitate exquisite (<50 nm) spatial resolution[32] for applications utilizing the diamond pillar as a probe for atomic force microscopy (AFM).[33,34] Several generations of devices have been explored in the literature, including cylinders,[31] truncated cones,[35−37] and parabolic reflectors.[38,39] Despite this progress, further optimizing the device geometry represents a key challenge in improving optical spin-readout efficiency and measurement sensitivity.

In this work, we realize an optimized diamond nanopillar for quantum sensing with the NV center. Starting with a truncated-cone design[35] (Figure 1a), we develop near-field optical simulations to explore the role of pillar geometry on collection efficiency. Specifically, we explore the impact of pillar height for the first time, finding a substantial improve-

Received: June 6, 2023
Revised: October 20, 2023
Accepted: October 24, 2023
Published: November 7, 2023

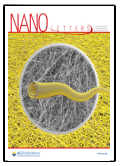

https://doi.org/10.1021/acs.nanolett.3c02120
Nano Lett. 2023, 23, 10110–10117

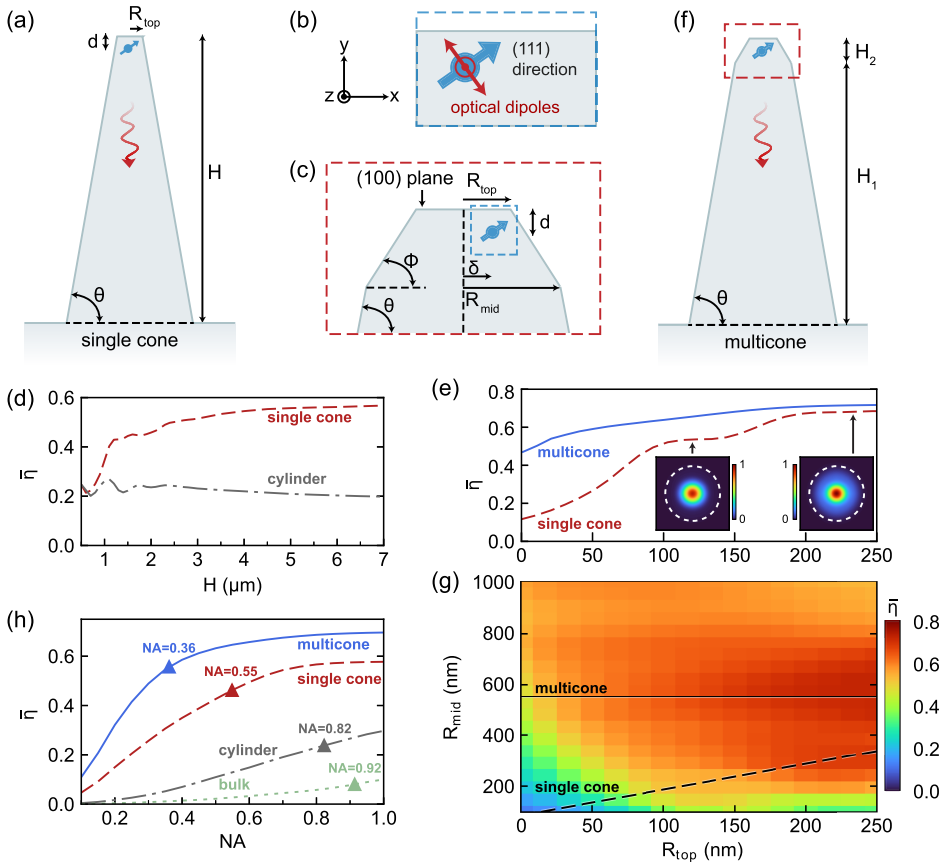

Figure 1. Nanopillar design and simulations. (a) Schematic of the single-cone geometry. (b) Illustration of an NV center oriented along the [111] crystal axis. (c) Example pillar facet including two distinct sidewall angles (θ, ϕ), i.e., the multicone geometry. (d) Collection efficiency $\overline{\eta}$ as a function of H for single-cone and cylinder geometries (R_{top} = 150 nm for both). (e) $\overline{\eta}$ as a function of R_{top} for the single-cone (dashed) and multicone (solid) geometries (H = 5 μm for both). Far-field intensity distributions (in air) are plotted for the single cone for R_{top} = 123 and 238 nm. Circles corresponding to the experimental NA = 0.75 are overlaid. (f) Schematic of the multicone geometry. (g) $\overline{\eta}$ as a function of R_{top} and R_{mid} for a multicone device. We consider two sidewall angles (fixed θ = 80° and varying ϕ) with H_1 = 4.5 μm and H_2 = 0.5 μm, respectively. Lines corresponding to the single-cone and multicone structures in (e) are overlaid. (h) $\overline{\eta}$ vs NA for three pillar geometries (R_{top} = 150 nm and H = 5 μm) and bulk diamond. Triangles indicate $NA_{0.80}$, the NA at which 80% of the intensity for NA = 1 is collected.

ment in the fluorescence collimation for tall structures. Next, we observe that collimation and emission directionality are enhanced by incorporating a shallow sidewall angle near the pillar facet. A representative set of structures is then created using a new fabrication process that is both simple and reliable. Subsequent optical characterization confirms our theoretical predictions, yielding a maximum spin-readout SNR of 0.106 for the optimized geometry, a factor-of-three improvement over a cylindrical device of similar dimensions. Moving forward, this work will facilitate a new generation of NV quantum sensing devices with superior sensitivity and exceptional spatial resolution.

We simulate the optical properties of diamond nanopillars using a finite-difference time-domain software from Lumerical Inc.[40] As a figure of merit, we calculate the wavelength-dependent collection efficiency $\eta(\lambda)$ normalized to the NV emission spectrum at room temperature $I(\lambda)$,[41] yielding

$$\overline{\eta} = \frac{\int_{\lambda_{coll}} \eta(\lambda) I(\lambda)\, d\lambda}{\int_{\lambda_{coll}} I(\lambda)\, d\lambda} \quad (1)$$

Here, we consider free-space optical collection from the pillar's base with numerical aperture NA = 0.75 and bandwidth λ_{coll} = 650−800 nm (matching our experimental setup). Individual NVs are modeled as two orthogonal electric dipoles located in the plane perpendicular to the [111] direction of a (100)-cut diamond (Figure 1b).[42] We assume all defects are located d = 5 nm below the pillar facet and centered laterally within the structure (δ = 0, Figure 1c). We observe only a slight variation in $\overline{\eta}$ over the range of possible emitter positions (see see Figure S2 in the Supporting Information).

Our starting point for developing an optimized nanopillar is the truncated-cone geometry (hereafter termed the "single cone" or SC),[35,37] which is fully parametrized by the top radius R_{top}, height H, and sidewall angle θ (Figure 1a). First, we explore the impact of H on $\overline{\eta}$ for R_{top} = 150 nm and θ = 80° (Figure 1d). We limit our study to H = 1−7 μm, which is the range over which we can achieve a high fabrication yield (larger H and smaller R_{top} result in device breakage). Meanwhile, θ was chosen to match the results of our standard fabrication process, yielding θ = 78°−86° (details below).

The SC exhibits a substantial increase in $\overline{\eta}$ vs H that saturates for $H \gtrsim 5$ μm, which can be attributed to the adiabatic expansion of the beam as it propagates down the structure.[39,43,44] Indeed, at the bulk−diamond interface, the waveguide has expanded by a factor of $\Delta \approx 1 + H \cot \theta / R_{top}$, reducing the divergence angle of the exiting beam by a similar factor (in the paraxial limit). In contrast, an equivalent

https://doi.org/10.1021/acs.nanolett.3c02120
Nano Lett. 2023, 23, 10110−10117

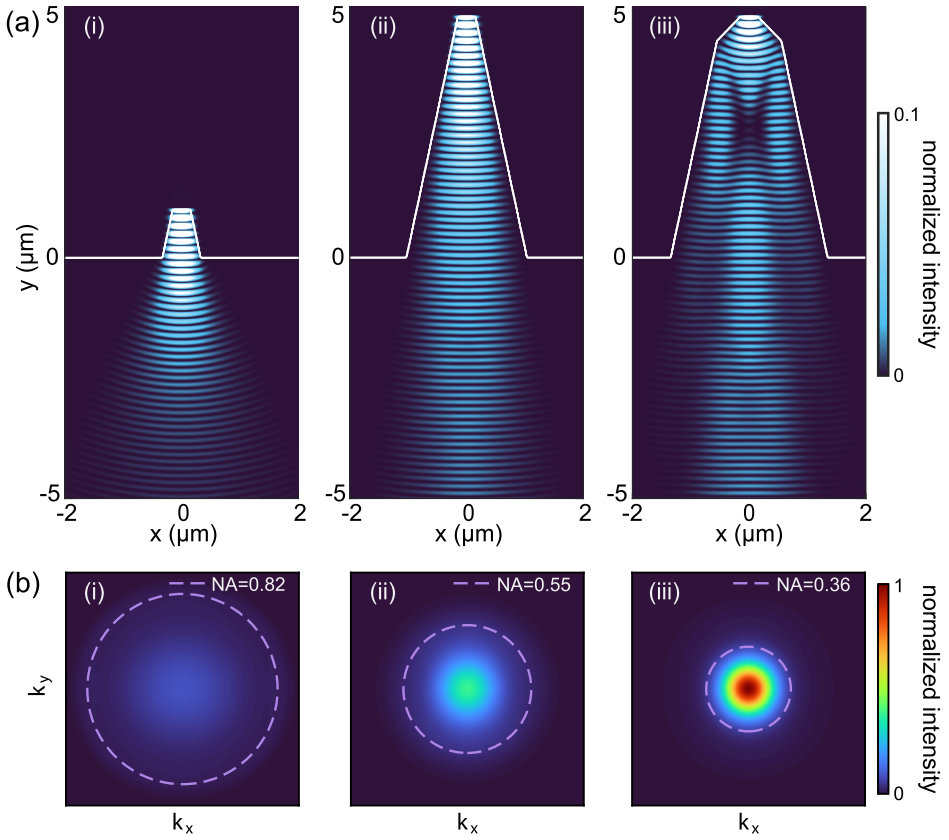

Figure 2. Mode simulations. (a) Propagating optical intensity for a fundamental-mode source (700 nm) in the diamond at the pillar facet (R_{top} = 150 nm) for a (i) 1 μm tall single cone, (ii) 5 μm tall single cone, and (iii) 5 μm tall multicone. Color bars are saturated at 0.1 of the maximum intensity for each device to increase visibility. (b) Far-field intensity showing the simulated angular distribution of NV emission for the geometries in (a) normalized to the maximum intensity of the MC structure (b(iii)). Purple dashed lines indicate $NA_{0.80}$, the NA yielding 80% of the collected intensity for NA = 1.

cylindrical pillar (θ = 90°, Figure 1d) exhibits a slight decay in $\overline{\eta}$ for tall structures. To the best of our knowledge, this is the first study exploring the critical impact of tapered pillar height on collection efficiency. Moreover, the tapered sidewalls of the SC increase total internal reflection at the top of the device, facilitating $\overline{\eta}$ > 0.5. Consequently, we target H = 5 μm to achieve a high collection efficiency and fabrication yield.

Next, we observe a monotonic increase in $\overline{\eta}$ as a function of R_{top} (Figure 1e). Specifically, $\overline{\eta}$ increases rapidly for small R_{top} and plateaus at ≈0.5 for R_{top} = 100−150 nm, corresponding to the radii at which the waveguide supports fundamental modes within the NV spectrum. Efficiency continues to increase for R_{top} > 150 nm with further plateaus corresponding to higher-order transverse modes. However, for scanning applications, it is desirable to reduce R_{top} to maximize the spatial resolution. Thus, we target R_{top} = 150 nm as a compromise between high $\overline{\eta}$, device yield, and spatial resolution.

Inspired by recent results showing that a parabolic structure can improve collection efficiency,[38,39] we explore the impact of introducing an additional sidewall angle ϕ near the facet (Figures 1c and 1f), yielding a "multicone" (MC) structure. Again, we consider a 5 μm tall device with a lower region (H_1 = 4.5 μm) defined by our standard fabrication procedure (θ = 80°) and an upper part (H_2 = 0.5 μm) with varying sidewall angle ϕ. Equivalently, the upper region can be parametrized by the radius at the interface between regions $R_{mid} = R_{top} + H_2 \cot \phi$. We simulate $\overline{\eta}$ for varying R_{top} and R_{mid} (Figure 1g) and overlay a dashed line corresponding to the SC (ϕ = 80°) for comparison. We observe that for every R_{top}, an MC geometry with $\phi < \theta$ exists yielding larger $\overline{\eta}$. Moreover, the parameter space for improved efficiency is relatively large ($\overline{\eta}$ > 0.6 for R_{top} = 130−250 nm and ϕ = 40°−80°), providing generous fabrication tolerances.

Like the SC, the improvement in $\overline{\eta}$ for the MC can be partially ascribed to the increased mode diameter at the pillar's base. However, introducing a shallow sidewall angle at the facet also increases the reflection at this interface and, thereby, the directionality of emission. To gain further insight into the role of R_{top}, we overlay a solid line in Figure 1g for R_{mid} = 550 nm and plot the corresponding $\overline{\eta}$ in Figure 1e. In contrast to the plateaus observed for the SC, the MC exhibits a relatively smooth increase in $\overline{\eta}$ vs R_{top} due to transverse-mode mixing; indeed, the reduced sidewall angle no longer fulfills the adiabatic expansion criteria.[45,46] This ability to support additional transverse modes further increases $\overline{\eta}$ for free-space or multimode collection.

We summarize our pillar optimization by plotting $\overline{\eta}$ vs NA for a cylinder, SC, MC, and bulk diamond (Figure 1h). As expected, the MC yields the highest collection efficiency for NA in the range [0.1, 1]. While these efficiencies are comparable to those achieved with previously reported pillar designs,[37,38] we emphasize that the MC is optimized for near-surface NV centers suitable for quantum sensing. We compare the collimation of each structure by calculating $NA_{0.80}$, the NA yielding 80% of the collected intensity for NA = 1 (triangular markers in Figure 1h). The MC exhibits the best performance

https://doi.org/10.1021/acs.nanolett.3c02120
Nano Lett. 2023, 23, 10110−10117

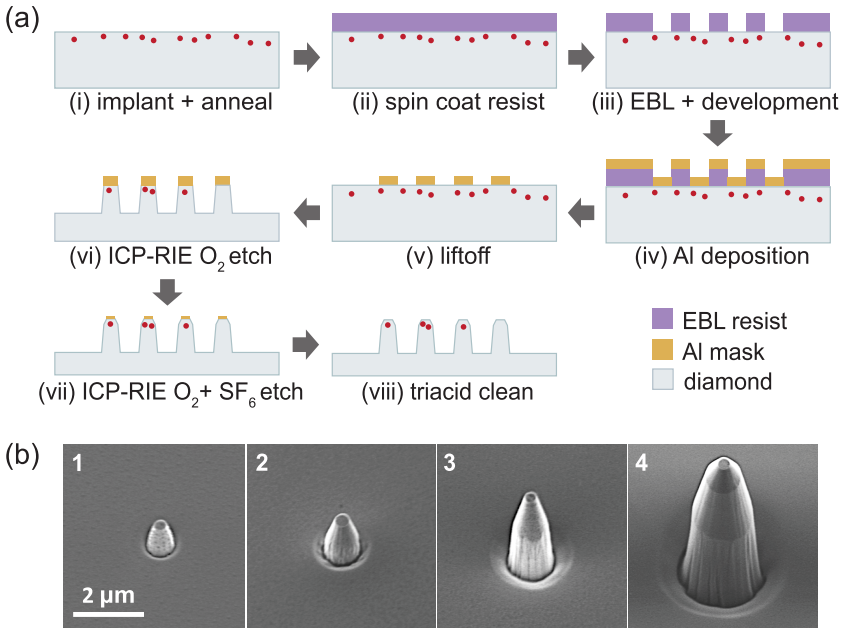

Figure 3. Nanofabrication process. (a) Pillar fabrication process flow (details in the main text and the Supporting Information). (b) Scanning electron microscopy (SEM) images of fabricated pillar geometries. Pillars 1−3 were etched using an O_2 chemistry, while pillar 4 was processed with O_2 plasma followed by a mixture of O_2 and SF_6.

with $NA_{0.80}$ = 0.36, which is very promising for future applications because compatibility with low-NA collection optics reduces experimental costs and complexity.

To verify the design principles obtained from Figure 1, we simulate the propagating intensity of a 700 nm fundamental-mode excitation at the pillar facet for three representative structures (Figure 2a), including two SCs of different heights and one MC. As expected, the SCs (Figures 2a(i,ii)) exhibit an adiabatic expansion of the mode as it travels down the structure.[45,46] For the 1 μm tall device, $\Delta \approx 2.2$; in contrast, the 5 μm tall pillar exhibits $\Delta \approx 6.9$ and superior collimation. The tall MC structure ($\phi = 51°$ and $H_1 = 4.5$ μm, Figure 2a(iii)) facilitates rapid modal expansion ($\Delta \approx 9.0$) and transverse-mode conversion.[45,46] While the reduction in divergence angle depends on the exact modal composition, the exiting beam exhibits flatter wavefronts than an SC of the same height (Figure 2a(ii)).

Finally, we simulate the far-field intensities for NV emission within the same geometries (Figure 2b; see the Supporting Information for wavelength-dependent plots). Here, we normalize all plots to the maximum value obtained for the MC and overlay circles corresponding to $NA_{0.80}$. As expected, a superior collimation is obtained for the tall MC structure. Moreover, despite the presence of higher-order transverse modes, the far-field emission remains approximately Gaussian and highly compatible with fiber-coupled applications.

We verify our simulation results by fabricating four representative pillar geometries for experimental characterization (see the Supporting Information for further fabrication details). To ensure consistent material properties, all devices are created from the same diamond crystal sliced into 20 μm thick membranes (facilitating optical collection through the substrate). Figure 3a illustrates the fabrication process flow: first, a high-quality diamond surface is prepared using an inductively coupled plasma reactive-ion etching (ICP RIE) process, relieving crystal strain and smoothing the surface to <0.2 nm rms. The substrate is then cleaned in a boiling triacid mixture (1:1:1 ratio of HNO_3, H_2SO_4, and $HClO_4$) and implanted with ^{15}N ions. Finally, nitrogen is converted to 5 ± 2 nm deep[47] NV centers via high-vacuum annealing.

Next, we lithographically define four pillar geometries (pillars 1−4, Figure 3b) using a layered electron-beam resist, followed by electron-beam lithography. Specifically, we pattern circles with radii of 200, 275, 400, and 650 nm (for pillars 1−4, respectively). Following development, aluminum masks are deposited by electron-beam evaporation and transferred into the diamond by ICP RIE (details below). Etching is terminated when $R_{top} \approx 150$ nm, which is determined using scanning electron microscopy (SEM); consequently, the height of the final structure is determined by the initial mask diameter. After etching, aluminum masks are removed in a triacid mixture.

Pillars 1−3 are created using an O_2-plasma recipe interrupted by SF_6 plasma to avoid micromasking. Initially, this process reduces the mask height, while the diameter is mainly unaffected, resulting in SC structures with $\theta = 78°-86°$. This modality is used to fabricate pillar geometries 1 and 2 (Figure 3b(i,ii)), with H = 1.3 μm and H = 1.8 μm, respectively. However, prolonged plasma exposure causes lateral mask erosion, which reduces the sidewall angle and forms MC structures.[48] Indeed, pillar 3 is fabricated using the same plasma recipe but exhibits a second, shallow sidewall angle with $\phi = 78°$ (Figure 3b(iii), $H_1 = 2.1$ μm and $H_2 = 1.9$ μm).

While promising, the fabrication of MC structures by mask erosion is difficult to control and requires constant monitoring with SEM. Consequently, we develop an alternative method for achieving a second, shallow sidewall angle based on new plasma chemistry (4:1 flow ratio of O_2 and SF_6) with different etch selectivity. We created the MC in Figure 3b(iv) by first etching with the O_2 recipe ($H_1 = 5.2$ μm), followed by the new plasma mixture (H_2 = 0.9 μm). Interestingly, the resulting structure exhibits two additional sidewall angles: $\phi = 64°$ (H = 5.2−6.1 μm) from the new chemistry and $\phi = 82°$ (H = 2.9−

https://doi.org/10.1021/acs.nanolett.3c02120
Nano Lett. 2023, 23, 10110−10117

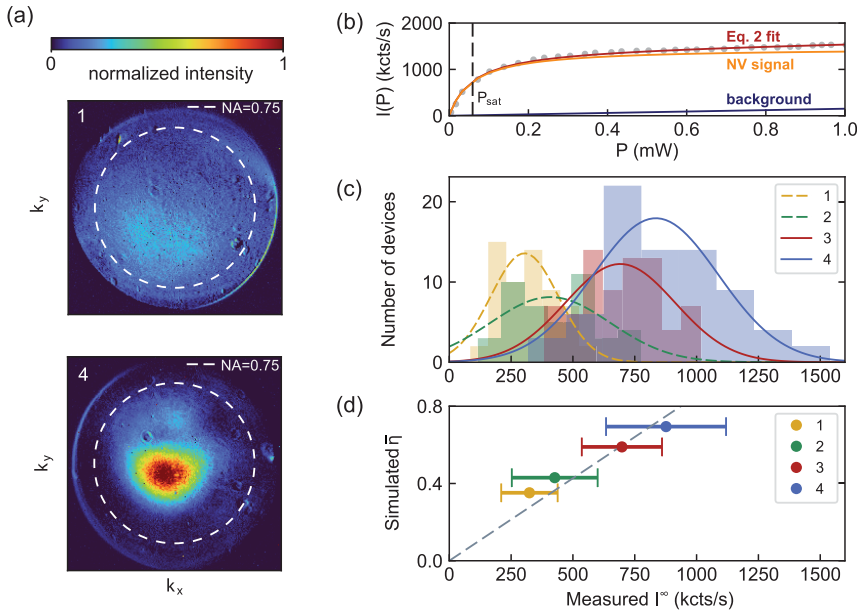

Figure 4. Experimental characterization. (a) Back-focal-plane images of representative pillar 1 and 4 devices. Measurements are normalized to the peak intensity of pillar 4, and dashed circles corresponding to NA = 0.75 are overlaid. (b) An example fluorescence saturation measurement for a multicone device (pillar 4) fit with eq 2 (P_{sat} = 59 ± 2 μW, I^{∞} = 1464.9 ± 9.8 kcts/s). (c) Histogram showing the number of viable devices vs I^{∞} for the four geometries with Gaussian fits. (d) Simulated $\bar{\eta}$ vs measured I^{∞} for each geometry with a linear fit overlaid. A similar relative uncertainty was obtained for all devices.

5.2 μm) caused by mask erosion during the O_2 process. Simulations of this structure suggest that the additional tapering further improves the directionality and collimation of the output beam.

Nanopillars are characterized using a home-built confocal microscope (see the Supporting Information for details). First, we identify devices containing single NVs from intensity autocorrelation measurements.[49] We survey over 400 pillars of each geometry, yielding 59, 43, 73, and 74 viable structures for geometries 1−4, respectively. Back-focal-plane imaging is employed to assess the difference in collimation between structures. Figure 4a shows the angular intensity distribution of representative pillar 1 and 4 devices, verifying that the optimized MC exhibits superior collimation.

Next, we compare the performance of each structure by measuring the NV fluorescence at an infinite pump power (I^{∞}), which scales linearly with $\bar{\eta}$. I^{∞} is obtained by fitting power-dependent fluorescence measurements (Figure 4b) to

$$I(P) = I^{\infty}\frac{P}{P + P_{sat}} + c_{bg}P \tag{2}$$

I is the measured count rate, P is the excitation power, P_{sat} is the fitted saturation power, and c_{bg} is a linear background contribution. Critically, saturation measurements allow us to account for variations in the excitation power between devices. The results are illustrated in a histogram (Figure 4c) showing the number of devices vs I^{∞} for the four geometries; the increase in collection intensity afforded by tall pillars and the MC geometry confirms our simulation predictions. A quantitative comparison can be gained by plotting simulated $\bar{\eta}$ against measured I^{∞} for each test geometry (Figure 4d), yielding a linear relationship with slope (850 ± 50) × 10^{-6} s/kct.

Finally, we assess the potential of our optimized structures for NV quantum sensing. We consider an experiment where the measured signal is encoded in the populations of two ground-state spin sublevels, denoted $|0\rangle$ and $|1\rangle$. These populations can be discriminated by their integrated spin-dependent fluorescence, α_0 and α_1, due to the optical contrast between spin states ($C = 1 - \alpha_1/\alpha_0$). Typically, $\alpha_{0/1} \ll 1$ for off-resonant optical readout, and measurements are dominated by shot noise, yielding a single-measurement spin-readout SNR of[50]

$$\mathrm{SNR} \approx \sqrt{\alpha_0}\frac{C}{\sqrt{2 - C}} \tag{3}$$

We estimate this quantity for a representative pillar 4 device by measuring α_0 and C at different laser powers (circular markers in Figure 5; see the Supporting Information for details). Here, we apply a small magnetic field ($B \approx 2$ mT) along the NV axis to lift the degeneracy of the $m_s = \pm 1$ ground states and work

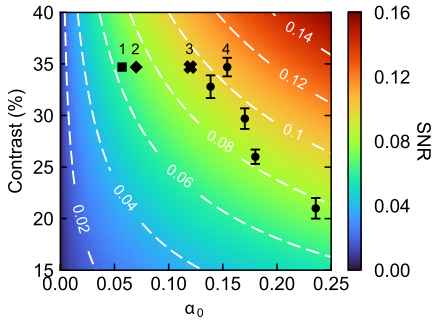

Figure 5. Measured optical contrast (C) vs integrated photon counts per measurement (α_0) for a representative pillar 4 device at five different excitation powers (circular markers). The corresponding spin-readout SNR is calculated and overlaid in a color plot. The maximum experimental SNR = 0.106 is obtained for α_0 = 0.154 and C = 34.7 ± 0.9%. For comparison, we estimate the corresponding maximum SNR for pillars 1−3 as 0.064 (squares), 0.073 (diamonds), and 0.095 (crosses), respectively.

https://doi.org/10.1021/acs.nanolett.3c02120
Nano Lett. 2023, 23, 10110−10117

within the $m_s = -1$ ($|1\rangle$) and $m_s = 0$ ($|0\rangle$) manifold. We estimate C at each laser power by fitting power-dependent Rabi experiments and calculate the average α_0 per measurement by integrating the spin-dependent fluorescence for a fixed measurement time $T_m = 300$ ns. While we use a fixed value for simplicity, T_m can be optimized at each laser power to maximize SNR.[51] We then overlay the calculated values from eq 3 for comparison, yielding a maximum SNR = 0.106 for $C = 34.7 \pm 0.9\%$ and $\alpha_0 = 0.154$ photons/measurement. Promisingly, an SNR of 1 could be achieved by integrating only 90 measurements.

For comparison, we estimate the corresponding peak SNR for pillars 1−3 (Figure 5). Here, we assume the same optical contrast of $C = 34.7 \pm 0.9\%$ because the internal NV dynamics and background fluorescence should not change between device geometries.[35] Moreover, we scale $\alpha_0 = 0.154$ by the ratio of average I^∞ values obtained for each structure (Figure 4d), resulting in a spin-readout SNR of 0.064, 0.073, and 0.095 for pillars 1−3, respectively. Consequently, pillar 4 should exhibit a factor-of-three reduction in measurement time to obtain the same SNR as pillar 1.

This work presents a diamond nanopillar structure that is optimized for NV sensing experiments. We perform the first systematic study showing superior performance for tall ($H \geq 5$ μm) truncated-cone structures, which is further enhanced by additional tapering near the facet. Next, we develop a novel fabrication process and create four representative test devices; subsequent optical characterization verifies our design principles, yielding a factor-of-20 improvement in collection efficiency for an optimized device compared to bulk diamond and a single-measurement spin-readout SNR = 0.106.

The improved performance of this optimized device will significantly benefit future quantum-sensing technologies. Beyond experimental speedup, SNR improves the magnetic sensitivity.[52] In addition, the spatial resolution of the MC could be further optimized for AFM measurements by reducing R_{top}; indeed, $\overline{\eta} > 0.5$ for radii approaching 20 nm. Finally, the resulting beam of the optimized MC device is highly Gaussian and collimated, compatible with free-space or fiber-coupled technologies utilizing low-NA collection optics.

Beyond NV centers, the devices developed here could be easily translated to alternative diamond defects, including the negatively charged group IV emitters[53] and other emerging color centers.[54,55] Finally, our design principles also apply to emitters in alternative materials, such as defect centers in SiC[56] or rare-earth ions in doped glasses.[57]

■ ASSOCIATED CONTENT

Supporting Information

The Supporting Information is available free of charge at https://pubs.acs.org/doi/10.1021/acs.nanolett.3c02120.

Additional information on wavelength-dependent simulations, fabrication details, the experimental setup, NV-displacement simulations, single-photon measurements, back-focal-plane imaging, and Rabi-oscillation measurements (PDF)

■ AUTHOR INFORMATION

Corresponding Authors

Christian L. Degen − *Department of Physics, ETH Zürich, 8093 Zürich, Switzerland;* orcid.org/0000-0003-2432-4301; Email: degenc@ethz.ch

Erika Janitz − *Department of Electrical and Software Engineering, University of Calgary, Calgary, AB, Canada T2N 1N4;* orcid.org/0000-0003-3299-9165; Email: erika.janitz@ucalgary.ca

Authors

Tianqi Zhu − *Department of Physics, ETH Zürich, 8093 Zürich, Switzerland;* orcid.org/0009-0004-8154-6984

Jan Rhensius − *QZabre LLC, 8050 Zürich, Switzerland*

Konstantin Herb − *Department of Physics, ETH Zürich, 8093 Zürich, Switzerland*

Viraj Damle − *QZabre LLC, 8050 Zürich, Switzerland*

Gabriel Puebla-Hellmann − *QZabre LLC, 8050 Zürich, Switzerland*

Complete contact information is available at: https://pubs.acs.org/10.1021/acs.nanolett.3c02120

Notes

The authors declare no competing financial interest.

■ ACKNOWLEDGMENTS

The authors thank Stefan Ernst, Zhewen Xu, Marius Palm, Pol Welter, Mihai Gabureac, Simon Josephy, William Huxter, Andrea Morales, Laura Alicia Völker, and John Abendroth for fruitful discussions. This work was supported by the European Research Council through ERC CoG 817720 (IMAGINE), the Swiss National Science Foundation (SNSF) through Project Grant No. 200020-175600 and NCCR QSIT, a National Centre of Competence in Research in Quantum Science and Technology, Grant No. 51NF40-185902, and the Advancing Science and TEchnology thRough dIamond Quantum Sensing (ASTERIQS) program, Grant No. 820394, of the European Commission. E.J. acknowledges support from a Natural Sciences and Engineering Research Council of Canada (NSERC) postdoctoral fellowship (PDF-558200-2021).

■ REFERENCES

(1) Aharonovich, I.; Englund, D.; Toth, M. Solid-State Single-Photon Emitters. *Nat. Photonics* **2016**, *10*, 631−641.

(2) Schirhagl, R.; Chang, K.; Loretz, M.; Degen, C. L. Nitrogen-Vacancy Centers in Diamond: Nanoscale Sensors for Physics and Biology. *Annu. Rev. Phys. Chem.* **2014**, *65*, 83−105.

(3) Doherty, M. W.; Manson, N. B.; Delaney, P.; Jelezko, F.; Wrachtrup, J.; Hollenberg, L. C. The Nitrogen-Vacancy Colour Centre in Diamond. *Phys. Rep.* **2013**, *528*, 1−45.

(4) Gross, I.; Akhtar, W.; Garcia, V.; Martínez, L.; Chouaieb, S.; Garcia, K.; Carrétéro, C.; Barthélémy, A.; Appel, P.; Maletinsky, P.; et al. Real-Space Imaging of Non-Collinear Antiferromagnetic Order with a Single-Spin Magnetometer. *Nature* **2017**, *549*, 252−256.

(5) Thiel, L.; Wang, Z.; Tschudin, M. A.; Rohner, D.; Gutiérrez-Lezama, I.; Ubrig, N.; Gibertini, M.; Giannini, E.; Morpurgo, A. F.; Maletinsky, P. Probing Magnetism in 2D Materials at the Nanoscale with Single-Spin Microscopy. *Science* **2019**, *364*, 973−976.

(6) Chang, K.; Eichler, A.; Rhensius, J.; Lorenzelli, L.; Degen, C. L. Nanoscale Imaging of Current Density with a Single-Spin Magnetometer. *Nano Lett.* **2017**, *17*, 2367−2373.

(7) Lovchinsky, I.; Sushkov, A. O.; Urbach, E.; de Leon, N. P.; Choi, S.; De Greve, K.; Evans, R.; Gertner, R.; Bersin, E.; Müller, C.; et al. Nuclear Magnetic Resonance Detection and Spectroscopy of Single Proteins Using Quantum Logic. *Science* **2016**, *351*, 836−841.

(8) Herbschleb, E. D.; Kato, H.; Maruyama, Y.; Danjo, T.; Makino, T.; Yamasaki, S.; Ohki, I.; Hayashi, K.; Morishita, H.; Fujiwara, M.; Mizuochi, N.; et al. Ultra-Long Coherence Times amongst Room-Temperature Solid-State Spins. *Nat. Commun.* **2019**, *10*, 3776.

(9) Abobeih, M. H.; Cramer, J.; Bakker, M. A.; Kalb, N.; Markham, M.; Twitchen, D. J.; Taminiau, T. H. One-Second Coherence for a Single Electron Spin Coupled to a Multi-Qubit Nuclear-Spin Environment. *Nat. Commun.* **2018**, *9*, 2552.
(10) Robledo, L.; Bernien, H.; Van Der Sar, T.; Hanson, R. Spin Dynamics in the Optical Cycle of Single Nitrogen-Vacancy Centres in Diamond. *New J. Phys.* **2011**, *13*, 025013.
(11) Rong, X.; Geng, J.; Shi, F.; Liu, Y.; Xu, K.; Ma, W.; Kong, F.; Jiang, Z.; Wu, Y.; Du, J. Experimental Fault-Tolerant Universal Quantum Gates with Solid-State Spins under Ambient Conditions. *Nat. Commun.* **2015**, *6*, 8748.
(12) Taylor, J. M.; Cappellaro, P.; Childress, L.; Jiang, L.; Budker, D.; Hemmer, P. R.; Yacoby, A.; Walsworth, R.; Lukin, M. D. High-Sensitivity Diamond Magnetometer with Nanoscale Resolution. *Nat. Phys.* **2008**, *4*, 810−816.
(13) Castelletto, S.; et al. Diamond-Based Structures to Collect and Guide Light. *New J. Phys.* **2011**, *13*, 025020.
(14) Castelletto, S.; Rosa, L.; Blackledge, J.; Al Abri, M. Z.; Boretti, A. Advances in Diamond Nanofabrication for Ultrasensitive Devices. *Microsyst. Nanoeng.* **2017**, *3*, 1−16.
(15) Schröder, T.; Mouradian, S. L.; Zheng, J.; Trusheim, M. E.; Walsh, M.; Chen, E. H.; Li, L.; Bayn, I.; Englund, D. Quantum Nanophotonics in Diamond. *JOSA B* **2016**, *33*, B65−B83.
(16) Choy, J. T.; Hausmann, B. J. M.; Babinec, T. M.; Bulu, I.; Khan, M.; Maletinsky, P.; Yacoby, A.; Lončar, M. Enhanced Single-Photon Emission from a Diamond−Silver Aperture. *Nat. Photonics* **2011**, *5*, 738−743.
(17) Park, Y.-S.; Cook, A. K.; Wang, H. Cavity QED with Diamond Nanocrystals and Silica Microspheres. *Nano Lett.* **2006**, *6*, 2075−2079.
(18) Chakravarthi, S.; Chao, P.; Pederson, C.; Molesky, S.; Ivanov, A.; Hestroffer, K.; Hatami, F.; Rodriguez, A. W.; Fu, K.-M. C. Inverse-Designed Photon Extractors for Optically Addressable Defect Qubits. *Optica* **2020**, *7*, 1805−1811.
(19) Englund, D.; Shields, B.; Rivoire, K.; Hatami, F.; Vučković, J.; Park, H.; Lukin, M. D. Deterministic Coupling of a Single Nitrogen Vacancy Center to a Photonic Crystal Cavity. *Nano Lett.* **2010**, *10*, 3922−3926.
(20) Wambold, R. A.; Yu, Z.; Xiao, Y.; Bachman, B.; Jaffe, G.; Kolkowitz, S.; Choy, J. T.; Eriksson, M. A.; Hamers, R. J.; Kats, M. A. Adjoint-Optimized Nanoscale Light Extractor for Nitrogen-Vacancy Centers in Diamond. *Nanophotonics* **2020**, *10*, 393−401.
(21) Lončar, M.; Faraon, A. Quantum Photonic Networks in Diamond. *MRS Bull.* **2013**, *38*, 144−148.
(22) Bai, D.; Capelli, M.; Huynh, H.; Ebendorff-Heidepriem, H.; Foster, S.; Greentree, A. D.; Gibson, B. C. Hybrid Diamond-Glass Optical Fibres for Magnetic Sensing. *26th Int. Conf. Opt. Fiber Sens. 2018 Pap. WD3.* **2018**, WD3.
(23) Burek, M. J.; Chu, Y.; Liddy, M. S.; Patel, P.; Rochman, J.; Meesala, S.; Hong, W.; Quan, Q.; Lukin, M. D.; Lončar, M. High Quality-Factor Optical Nanocavities in Bulk Single-Crystal Diamond. *Nat. Commun.* **2014**, *5*, 5718.
(24) Mitchell, M.; Lake, D. P.; Barclay, P. E. Realizing Q > 300 000 in Diamond Microdisks for Optomechanics via Etch Optimization. *APL Photonics* **2019**, *4*, No. 016101.
(25) Atikian, H. A.; Latawiec, P.; Burek, M. J.; Sohn, Y.-I.; Meesala, S.; Gravel, N.; Kouki, A. B.; Lončar, M. Freestanding Nanostructures via Reactive Ion Beam Angled Etching. *APL Photonics* **2017**, *2*, No. 051301.
(26) Hadden, J. P.; Harrison, J. P.; Stanley-Clarke, A. C.; Marseglia, L.; Ho, Y.-L. D.; Patton, B. R.; O'Brien, J. L.; Rarity, J. G. Strongly Enhanced Photon Collection from Diamond Defect Centers under Microfabricated Integrated Solid Immersion Lenses. *Appl. Phys. Lett.* **2010**, *97*, No. 241901.
(27) Huang, T.-Y.; Grote, R. R.; Mann, S. A.; Hopper, D. A.; Exarhos, A. L.; Lopez, G. G.; Klein, A. R.; Garnett, E. C.; Bassett, L. C. A Monolithic Immersion Metalens for Imaging Solid-State Quantum Emitters. *Nat. Commun.* **2019**, *10*, 2392.
(28) Li, L.; Chen, E. H.; Zheng, J.; Mouradian, S. L.; Dolde, F.; Schröder, T.; Karaveli, S.; Markham, M. L.; Twitchen, D. J.; Englund, D. Efficient Photon Collection from a Nitrogen Vacancy Center in a Circular Bullseye Grating. *Nano Lett.* **2015**, *15*, 1493−1497.
(29) Hausmann, B. J. M.; Shields, B. J.; Quan, Q.; Chu, Y.; de Leon, N. P.; Evans, R.; Burek, M. J.; Zibrov, A. S.; Markham, M.; Twitchen, D.; et al. Coupling of NV centers to photonic crystal nanobeams in diamond. *Nano Lett.* **2013**, *13*, 5791−5796.
(30) Hausmann, B. J.; Khan, M.; Zhang, Y.; Babinec, T. M.; Martinick, K.; McCutcheon, M.; Hemmer, P. R.; Lončar, M. Fabrication of diamond nanowires for quantum information processing applications. *Diamond Relat. Mater.* **2010**, *19*, 621−629.
(31) Babinec, T. M.; Hausmann, B. J. M.; Khan, M.; Zhang, Y.; Maze, J. R.; Hemmer, P. R.; Lončar, M. A Diamond Nanowire Single-Photon Source. *Nat. Nanotechnol.* **2010**, *5*, 195−199.
(32) Marchiori, E.; Ceccarelli, L.; Rossi, N.; Lorenzelli, L.; Degen, C. L.; Poggio, M. Nanoscale Magnetic Field Imaging for 2D Materials. *Nature Reviews Physics* **2022**, *4*, 49−60.
(33) Degen, C. L. Scanning Magnetic Field Microscope with a Diamond Single-Spin Sensor. *Appl. Phys. Lett.* **2008**, *92*, No. 243111.
(34) Maletinsky, P.; Hong, S.; Grinolds, M. S.; Hausmann, B.; Lukin, M. D.; Walsworth, R. L.; Loncar, M.; Yacoby, A. A Robust Scanning Diamond Sensor for Nanoscale Imaging with Single Nitrogen-Vacancy Centres. *Nat. Nanotechnol.* **2012**, *7*, 320−324.
(35) Momenzadeh, S. A.; Stöhr, R. J.; De Oliveira, F. F.; Brunner, A.; Denisenko, A.; Yang, S.; Reinhard, F.; Wrachtrup, J. Nanoengineered Diamond Waveguide as a Robust Bright Platform for Nanomagnetometry Using Shallow Nitrogen Vacancy Centers. *Nano Lett.* **2015**, *15*, 165−169.
(36) Torun, C. G.; Schneider, P.-I.; Hammerschmidt, M.; Burger, S.; Munns, J. H.; Schröder, T. Optimized diamond inverted nanocones for enhanced color center to fiber coupling. *Appl. Phys. Lett.* **2021**, *118*, No. 234002.
(37) Jeon, S.-W.; Lee, J.; Jung, H.; Han, S.-W.; Cho, Y.-W.; Kim, Y.-S.; Lim, H.-T.; Kim, Y.; Niethammer, M.; Lim, W. C.; et al. Bright nitrogen-vacancy centers in diamond inverted nanocones. *Acs Photonics* **2020**, *7*, 2739−2747.
(38) Wan, N. H.; Shields, B. J.; Kim, D.; Mouradian, S.; Lienhard, B.; Walsh, M.; Bakhru, H.; Schröder, T.; Englund, D. Efficient Extraction of Light from a Nitrogen-Vacancy Center in a Diamond Parabolic Reflector. *Nano Lett.* **2018**, *18*, 2787−2793.
(39) Hedrich, N.; Rohner, D.; Batzer, M.; Maletinsky, P.; Shields, B. J. Parabolic Diamond Scanning Probes for Single-Spin Magnetic Field Imaging. *Phys. Rev. Appl.* **2020**, *14*, No. 064007.
(40) Lumerical Inc. https://www.ansys.com/products/photonics (accessed 2023-04-28).
(41) Rondin, L.; Dantelle, G.; Slablab, A.; Grosshans, F.; Treussart, F.; Bergonzo, P.; Perruchas, S.; Gacoin, T.; Chaigneau, M.; Chang, H.-C.; Jacques, V.; Roch, J.-F. Surface-Induced Charge State Conversion of Nitrogen-Vacancy Defects in Nanodiamonds. *Phys. Rev. B* **2010**, *82*, No. 115449.
(42) Epstein, R. J.; Mendoza, F. M.; Kato, Y. K.; Awschalom, D. D. Anisotropic Interactions of a Single Spin and Dark-Spin Spectroscopy in Diamond. *Nat. Phys.* **2005**, *1*, 94−98.
(43) Munsch, M.; Malik, N. S.; Dupuy, E.; Delga, A.; Bleuse, J.; Gérard, J.-M.; Claudon, J.; Gregersen, N.; Mørk, J. Dielectric GaAs Antenna Ensuring an Efficient Broadband Coupling between an InAs Quantum Dot and a Gaussian Optical Beam. *Phys. Rev. Lett.* **2013**, *110*, No. 177402.
(44) Stepanov, P.; Delga, A.; Gregersen, N.; Peinke, E.; Munsch, M.; Teissier, J.; Mørk, J.; Richard, M.; Bleuse, J.; Gérard, J.-M.; Claudon, J. Highly Directive and Gaussian Far-Field Emission from "Giant" Photonic Trumpets. *Appl. Phys. Lett.* **2015**, *107*, No. 141106.
(45) Milton, A.; Burns, W. Mode Coupling in Optical Waveguide Horns. *IEEE J. Quantum Electron.* **1977**, *13*, 828−835.
(46) Fu, Y.; Ye, T.; Tang, W.; Chu, T. Efficient Adiabatic Silicon-on-Insulator Waveguide Taper. *Photon. Res.* **2014**, *2*, A41−A44.

https://doi.org/10.1021/acs.nanolett.3c02120
Nano Lett. 2023, 23, 10110−10117

(47) Ziegler, J. F.; Ziegler, M. D.; Biersack, J. P. SRIM−The Stopping and Range of Ions in Matter (2010). *Nucl. Instrum. Methods Phys. Res. Sect. B Beam Interact. Mater. At.* **2010**, *268*, 1818−1823.
(48) Forsberg, P.; Karlsson, M. Inclined Surfaces in Diamond: Broadband Antireflective Structures and Coupling Light through Waveguides. *Opt. Express* **2013**, *21*, 2693.
(49) Brouri, R.; Beveratos, A.; Poizat, J.-P.; Grangier, P. Photon Antibunching in the Fluorescence of Individual Color Centers in Diamond. *Opt. Lett.* **2000**, *25*, 1294−1296.
(50) Hopper, D. A.; Shulevitz, H. J.; Bassett, L. C. Spin Readout Techniques of the Nitrogen-Vacancy Center in Diamond. *Micromachines* **2018**, *9*, 437.
(51) Gupta, A.; Hacquebard, L.; Childress, L. Efficient Signal Processing for Time-Resolved Fluorescence Detection of Nitrogen-Vacancy Spins in Diamond. *JOSA B* **2016**, *33*, B28−B34.
(52) Janitz, E.; Herb, K.; Völker, L. A.; Huxter, W. S.; Degen, C. L.; Abendroth, J. M. Diamond Surface Engineering for Molecular Sensing with Nitrogen − Vacancy Centers. *J. Mater. Chem. C* **2022**, *10*, 13533−13569.
(53) Bradac, C.; Gao, W.; Forneris, J.; Trusheim, M. E.; Aharonovich, I. Quantum Nanophotonics with Group IV Defects in Diamond. *Nat. Commun.* **2019**, *10*, 5625.
(54) Rose, B. C.; Huang, D.; Zhang, Z.-H.; Stevenson, P.; Tyryshkin, A. M.; Sangtawesin, S.; Srinivasan, S.; Loudin, L.; Markham, M. L.; Edmonds, A. M.; et al. Observation of an Environmentally Insensitive Solid-State Spin Defect in Diamond. *Science* **2018**, *361*, 60−63.
(55) Mukherjee, S.; et al. A Telecom O-band Emitter in Diamond. *Nano Lett.* **2023**, *23*, 2557−2562.
(56) Lukin, D. M.; Guidry, M. A.; Vučković, J. Integrated Quantum Photonics with Silicon Carbide: Challenges and Prospects. *PRX Quantum* **2020**, *1*, No. 020102.
(57) Zhong, T.; Kindem, J. M.; Bartholomew, J. G.; Rochman, J.; Craiciu, I.; Verma, V.; Nam, S. W.; Marsili, F.; Shaw, M. D.; Beyer, A. D.; et al. Optically Addressing Single Rare-Earth Ions in a Nanophotonic Cavity. *Phys. Rev. Lett.* **2018**, *121*, No. 183603.

https://doi.org/10.1021/acs.nanolett.3c02120
Nano Lett. 2023, 23, 10110−10117